# Aeroelastic Analysis of Launch Vehicles in Transonic Flight

João Luiz F. Azevedo*
*Stanford University, Stanford, California*

**A numerical study of the aeroelastic stability of launch vehicles in transonic flight is performed. The unsteady aerodynamic flowfield about the vehicle is simulated using the three-dimensional Reynolds-averaged Navier-Stokes equations, accounting for turbulent mixing by a two-layer algebraic eddy viscosity model. The structural-dynamic formulation considers free-free flexural vibration of an elongated beam with variable properties, and the equations are cast in modal form. The two sets of equations are integrated simultaneously in time, after an initial perturbation, to ascertain the aeroelastic stability of a given configuration. The method proposed is described in detail and results that illustrate its application are presented. Steady-state pressure coefficient distributions show good agreement with available experimental data. Reasonable unsteady aerodynamic calculations and aeroelastic responses were obtained that still need further validation.**

## Nomenclature

$A, B, C$ = inviscid part of flux Jacobian matrices
$C_{cp}, C_{\text{Kleb}}, C_{wk}$ = constants used in the turbulence model
$Cp$ = pressure coefficient, $2/\gamma M^2\infty[(p/p\infty) - 1]$
$C_v$ = specific heat at constant volume
$e$ = total energy per unit of volume
$e_i$ = specific internal energy
$\bar{E}, \bar{F}, \bar{G}$ = flux vectors in Cartesian coordinates
$\hat{E}, \hat{F}, \hat{G}$ = flux vectors in body-conforming coordinates
$F(\eta), F_{\text{Kleb}}(\eta)$ = functions used in the turbulence model
$I$ = identity matrix
$J$ = Jacobian of the transformation
$k$ = reduced frequency
$K$ = constant used in the turbulence model
$l$ = length scale
$l(x, t)$ = running normal force
$L_\xi, L_\eta, L_\zeta$ = left-hand-side finite-difference operators
$m(x)$ = mass per unit of body length
$\bar{m}_i$ = generalized mass of the $i$th mode
$M$ = viscous part of flux Jacobian matrix
$M_\infty$ = freestream Mach number
$p$ = pressure
$P_i(t)$ = generalized aerodynamic force
$Pr$ = Prandtl number
$Pr_t$ = turbulent Prandtl number
$q_i$ = generalized modal coordinate
$q_x, q_y, q_z$ = Cartesian components of the heat flux vector
$\bar{Q}$ = vector of conserved quantities (Cartesian coordinates)
$\hat{Q}$ = vector of conserved quantities (body-conforming coordinates)
$Re$ = freestream Reynolds number
$R_\xi, R_\eta, R_\zeta$ = right-hand-side finite-difference operators
$t$ = time
$T$ = temperature
$u, v, w$ = Cartesian components of fluid velocity
$x, y, z$ = Cartesian coordinates
$\alpha$ = angle of attack
$\gamma$ = ratio of specific heats
$\delta(x, t)$ = total deflection of the centerline
$\delta_{ij}$ = Kronecker delta
$\delta_\xi, \delta_\eta, \delta_\zeta$ = central difference operators
$\Delta_\xi, \Delta_\eta, \Delta_\zeta, \Delta_t$ = forward difference operators
$\nabla_\xi, \nabla_\eta, \nabla_\zeta$ = backward difference operators
$\varepsilon_E$ = artificial dissipation coefficient for explicit side
$\varepsilon_I$ = artificial dissipation coefficient for implicit side
$\zeta_i$ = modal damping coefficient
$\theta(t)$ = rigid body centerline angular deflection
$\theta_0$ = half-amplitude angle of the oscillation
$\mu_l$ = molecular (laminar) viscosity coefficient
$\mu_t$ = eddy (turbulent) viscosity coefficient
$\xi, \eta, \zeta$ = body conforming coordinates
$\rho$ = density
$\tau$ = time in the body conforming system
$\tau_{x_i x_j}$ = components of the viscous stress tensor
$\phi_i(x)$ = normal mode of vibration
$|\omega|$ = magnitude of vorticity vector
$\omega_i$ = natural frequency of the $i$th mode

## Introduction

THE transonic flight regime has always presented great difficulties to analysts, especially because of the inherent nonlinearities of the equations governing the flow at transonic speeds even in their most simplified form. Despite all its difficulties, the transonic regime is very important in aeronautical applications, and methods that would be able to perform routine aeroelastic analyses are necessary because current transport aircraft usually cruise in this regime and military aircraft maneuver in it. Even missiles, or launch vehicles in general, that usually are designed to acquire a very high speed in a reasonably short time have to pass safely through the transonic regime.

It is the purpose of this work to study the aeroelastic stability of hammerhead payloads, and other blunt geometries in general, during their transonic phase of flight. The interest in such types of vehicle geometries is related to the fact that they are sometimes very attractive options for the designer, but aeroelastic problems have been observed in the past[1-3] on certain vehicles with these configurations when passing through the transonic regime.

The classical approach for the analysis of the aeroelastic phenomena present in the transonic phase of flight of ballistic launch vehicles has been to use experimental data for the

Presented as Paper 87-0708 at the AIAA/ASME/ASCE/AHS 28th Structures, Structural Dynamics and Materials Conference, Monterey, CA, April 6-9, 1987; received June 5, 1987; revision received April 26, 1988. 

*Research Assistant, Department of Aeronautics and Astronautics; currently with Instituto de Atividades Espaciais, CTA, São José dos Campos, SP, Brazil. Member AIAA.

unsteady aerodynamic pressures together with some simplified structural-dynamic representation of the vehicle. This work presents an approach where use is made of the current computational fluid dynamics technology in order to perform such aeroelastic analyses by coupling the structural-dynamic equations representing the vehicle with some unsteady flow solver appropriate for the physical situation being treated.

The formulation of the aerodynamic problem will be presented next, followed by a discussion of how these equations are actually implemented in a computer program. The formulation of the aeroelastic problem will then be presented, and some applications of the present approach to the calculation of both the unsteady aerodynamic forces on rigid oscillating vehicles and the aeroelastic stability of elastic vehicles will be discussed. Finally, an attempt to identify the difficulties and advantages of this approach will be made, and some possible directions for improvements in the method will be suggested.

## Aerodynamic Formulation

For the physical situation under consideration, because of the complex shock-boundary-layer interaction and flow separation expected at transonic speeds, the appropriate set of flow equations that should be used are the three-dimensional Navier-Stokes equations. Since full solution of these equations around complex geometries is still beyond our computational capabilities, the method employed here solves the thin-layer approximation to the Reynolds-averaged Navier-Stokes equations, where the account for the turbulent mixing is done by the Baldwin and Lomax algebraic eddy viscosity model.[4]

The equations can be written in strong conservation-law form for three-dimensional Cartesian coordinates as:

$$\frac{\partial \boldsymbol{Q}}{\partial t}+\frac{\partial \boldsymbol{E}}{\partial x}+\frac{\partial \boldsymbol{F}}{\partial y}+\frac{\partial \boldsymbol{G}}{\partial z}=0 \tag{1}$$

where the vector of conserved quantities $\boldsymbol{Q}$ is

$$\boldsymbol{Q}=\begin{bmatrix}\rho\\ \rho u\\ \rho v\\ \rho w\\ e\end{bmatrix} \tag{2}$$

and the flux vectors $\boldsymbol{E}$, $\boldsymbol{F}$, and $\boldsymbol{G}$ are

$$\boldsymbol{E}=\begin{bmatrix}\rho u\\ \rho u^2+p-\tau_{xx}\\ \rho uv-\tau_{xy}\\ \rho uw-\tau_{xz}\\ (e+p-\tau_{xx})u-\tau_{xy}v-\tau_{xz}w+q_x\end{bmatrix} \tag{3}$$

$$\boldsymbol{F}=\begin{bmatrix}\rho v\\ \rho uv-\tau_{xy}\\ \rho v^2+p-\tau_{yy}\\ \rho vw-\tau_{yz}\\ (e+p-\tau_{yy})v-\tau_{xy}u+\tau_{yz}w+q_y\end{bmatrix} \tag{4}$$

$$\boldsymbol{G}=\begin{bmatrix}\rho w\\ \rho uw-\tau_{xz}\\ \rho vw-\tau_{yz}\\ \rho w^2+p-\tau_{zz}\\ (e+p-\tau_{zz})w-\tau_{xz}u-\tau_{yz}v+q_z\end{bmatrix} \tag{5}$$

The pressure $p$ is calculated by the equation of state for perfect gases

$$p=(\gamma-1)\rho e_i \tag{6}$$

where $e_i$ is the specific internal energy of the fluid

$$e_i=C_vT=\frac{e}{\rho}-\frac{1}{2}(u^2+v^2+w^2) \tag{7}$$

The Reynolds stress terms and turbulent heat flux terms that appear in the time-averaging process are accounted for by using the eddy-viscosity and eddy-conductivity concepts. By this approach the coefficients of viscosity and thermal conductivity are the sum of the molecular (laminar) part and the eddy (turbulent) part, and it is expected that this will model the turbulent mixing with sufficient accuracy for the problems addressed here. The components of the viscous stress tensor can then be written[5]:

$$\tau_{x_ix_j}=(\mu_l+\mu_t)\left(\frac{\partial u_i}{\partial x_j}+\frac{\partial u_j}{\partial x_i}\right)-\frac{2}{3}(\mu_l+\mu_t)\left(\frac{\partial u_k}{\partial x_k}\right)\delta_{ij} \tag{8}$$

where we have used a tensorial notation just because it affords greater generality in this case, and it should be clear that $(x_1, x_2, x_3)\equiv(x, y, z)$ and $(u_1, u_2, u_3)\equiv(u, v, w)$. The components of the heat-flux vector can be written (back in usual $x$, $y$, $z$ notation):

$$q_x=-\left(\frac{\mu_l}{Pr}+\frac{\mu_t}{Pr_t}\right)\gamma\frac{\partial e_i}{\partial x} \tag{9a}$$

$$q_y=-\left(\frac{\mu_l}{Pr}+\frac{\mu_t}{Pr_t}\right)\gamma\frac{\partial e_i}{\partial y} \tag{9b}$$

$$q_z=-\left(\frac{\mu_l}{Pr}+\frac{\mu_t}{Pr_t}\right)\gamma\frac{\partial e_i}{\partial z} \tag{9c}$$

The molecular viscosity coefficient $\mu_l$ was treated as a given constant throughout this work, but, conceptually, there is no difficulty in letting it be updated as the solution progresses by using, for example, the Sutherland viscosity relation. The eddy viscosity coefficient $\mu_t$ is obtained from the two-layer Baldwin and Lomax[4] algebraic model, which was implemented here in the usual way for wall-bounded shear layers[6,7] as

$$\mu_t=\begin{cases}(\mu_t)_{\text{inner}}, & \eta\le\eta_{\text{crossover}}\\ (\mu_t)_{\text{outer}}, & \eta>\eta_{\text{crossover}}\end{cases} \tag{10}$$

where $\eta$ is the distance normal from the wall, and $\eta_{\text{crossover}}$ is the smallest value of $\eta$ at which the inner and outer formulations give equal values.

The inner region uses the Prandtl-Van Driest formulation, such that

$$(\mu_t)_{\text{inner}}=\rho l^2|\omega| \tag{11}$$

where $|\omega|$ is the magnitude of the local vorticity vector, and the length scale $l$ is obtained

$$l=k\eta[1-\exp(-\eta^+/A^+)]$$

and $\eta^+=(\eta\sqrt{\rho_w\tau_w})/\mu_w$, $k=0.4$, $A^+=26$.

The formulation for the outer region is similar to a Clauser formulation and is given by

$$(\mu_t)_{\text{outer}}=KC_{cp}F_{\text{wake}}F_{\text{Kleb}}(\eta) \tag{12}$$

where

$$F_{\text{wake}}=\text{the smaller of}\begin{pmatrix}\eta_{\max}F_{\max}\\ C_{wk}\eta_{\max}\dfrac{U_{\text{dif}}^2}{F_{\max}}\end{pmatrix}$$

The values of $\eta_{\max}$ and $F_{\max}$ are obtained from the function

$$F(\eta)=\eta|\omega|\left[1-\exp\left(-\frac{\eta+}{A^+}\right)\right]$$

where $F_{\max}$ is the maximum value of $F(\eta)$ in the profile, and

$\eta_{max}$ is the value of $\eta$ at which it occurs. The function $F_{Kleb}(\eta)$, called the Klebanoff intermittency factor, is given by

$$F_{Kleb}(\eta) = [1 + 5.5(C_{Kleb}\eta/\eta_{max})^6]^{-1}$$

Finally, $U_{dif}$ is the difference between maximum and minimum total velocity in the profile (note that the minimum total velocity is zero for boundary layers), and the constants used have the following values: $K = 0.0168$, $C_{cp} = 1.6$, $C_{wk} = 0.25$, and $C_{Kleb} = 0.3$.

## Numerical Implementation

It is convenient, for the purpose of actually implementing the flow solver code, to have the governing equations transformed to a general body-conforming curvilinear coordinate system. This will make the formulation in the code independent of the details of the actual topology being solved, besides making it very convenient for applying the boundary conditions and implementing turbulence models. The transformation is known only numerically, which does not pose any difficulty since what one really wants to know are the metrics of the transformation and its Jacobian. The following generalized independent variable transformation[8,9] is used:

$$\tau = t \tag{13a}$$

$$\xi = \xi(x, y, z, t) \tag{13b}$$

$$\eta = \eta(x, y, z, t) \tag{13c}$$

$$\zeta = \zeta(x, y, z, t) \tag{13d}$$

It can be shown that the Navier-Stokes equations can still be written in conservation-law form in the new variables as

$$\frac{\partial \bar{Q}}{\partial \tau} + \frac{\partial \bar{E}}{\partial \xi} + \frac{\partial \bar{F}}{\partial \eta} + \frac{\partial \bar{G}}{\partial \zeta} = 0 \tag{14}$$

where

$$\bar{Q} = J^{-1}Q = J^{-1}\begin{bmatrix} \rho \\ \rho u \\ \rho v \\ \rho w \\ e \end{bmatrix} \tag{15a}$$

$$\bar{E} = J^{-1}(\xi_t Q + \xi_x E + \xi_y F + \xi_z G) \tag{15b}$$

$$F = J^{-1}(\eta_t Q + \eta_x E + \eta_y F + \eta_z G) \tag{15c}$$

$$\bar{G} = J^{-1}(\zeta_t Q + \zeta_x E + \zeta_y F + \zeta_z G) \tag{15d}$$

The Jacobian of the transformation, $J$, is given by

$$J = (x_\xi y_\eta z_\zeta + x_\eta y_\zeta z_\xi + x_\zeta y_\xi z_\eta - x_\xi y_\zeta z_\eta - x_\eta y_\xi z_\zeta - x_\zeta y_\eta z_\xi)^{-1}$$

and the metric terms are

$$\xi_x = J(y_\eta z_\zeta - y_\zeta z_\eta) \qquad \xi_y = J(x_\zeta z_\eta - x_\eta z_\zeta)$$

$$\xi_z = J(x_\eta y_\zeta - x_\zeta y_\eta) \qquad \eta_x = J(y_\zeta z_\xi - y_\xi z_\zeta)$$

$$\eta_y = J(x_\xi z_\zeta - x_\zeta z_\xi) \qquad \eta_z = J(x_\zeta y_\xi - x_\xi y_\zeta)$$

$$\zeta_x = J(y_\xi z_\eta - y_\eta z_\xi) \qquad \zeta_y = J(x_\eta z_\xi - x_\xi z_\eta)$$

$$\zeta_z = J(x_\xi y_\eta - x_\eta y_\xi) \qquad \xi_t = -x_\tau \xi_x - y_\tau \xi_y - z_\tau \xi_z$$

$$\eta_t = -x_\tau \eta_x - y_\tau \eta_y - z_\tau \eta_z \qquad \zeta_t = -x_\tau \zeta_x - y_\tau \zeta_y - z_\tau \zeta_z$$

In this work, $\eta$ is taken to be the direction normal (or almost normal) to the body. This is the only direction where the viscous effects are kept under the thin-layer approximation. It should be noted, however, that the code actually implemented has all the viscous terms in it, and the trimming down to the thin-layer approximation is done by the grid, which is too coarse in the other directions to capture the viscous effects.

The numerical algorithm used is the Beam and Warming implicit approximate factorization scheme[10] which, with three-point second-order central differencing used to approximate the space derivatives and the implicit Euler method used for the time-march, leads to the finite-difference equation:

$$L_\eta L_\zeta L_\xi \Delta_t \bar{Q} = R_\xi + R_\eta + R_\zeta \tag{16}$$

where the above operators are defined as[11,12]

$$L_\xi = (I + \Delta t \delta_\xi A^n - \varepsilon_I \Delta t J^{-1} \nabla_\xi \Delta_\xi J)$$

$$L_\eta = (I + \Delta t \delta_\eta C^n - \varepsilon_I \Delta t J^{-1} \nabla_\eta \Delta_\eta J - \Delta t Re^{-1} \bar{\delta}_\eta J^{-1} M^n J)$$

$$L_\zeta = (I + \Delta t \delta_\zeta B^n - \varepsilon_I \Delta t J^{-1} \nabla_\zeta \Delta_\zeta J)$$

$$R_\xi = -\Delta t \delta_\xi \bar{E}^n - \varepsilon_E \Delta t J^{-1} (\nabla_\xi \Delta_\xi)^2 J \bar{Q}^n$$

$$R_\eta = -\Delta t \delta_\eta \bar{F}^n - \varepsilon_E \Delta t J^{-1} (\nabla_\eta \Delta_\eta)^2 J \bar{Q}^n$$

$$R_\zeta = -\Delta t \delta_\zeta \bar{G}^n - \varepsilon_E \Delta t J^{-1} (\nabla_\zeta \Delta_\zeta)^2 J \bar{Q}^n$$

where $\delta_\xi$, $\delta_\eta$, and $\delta_\zeta$ are central difference operators; $\nabla_\xi$, $\nabla_\eta$, and $\nabla_\zeta$ are backward difference operators; and $\Delta_\xi$, $\Delta_\eta$, and $\Delta_\zeta$ are forward difference operators in the $\xi$, $\eta$, and $\zeta$ directions, respectively. The $\delta_\eta$ is a midpoint operator used to maintain a compact three-point second-order-accurate central difference scheme when differencing the viscous terms on the left-hand side. The $\Delta t$ is a forward difference operator in time, such that

$$\Delta t \bar{Q} = \bar{Q}^{n+1} - \bar{Q}^n$$

The quantities $\bar{Q}$, $\bar{E}$, $\bar{F}$ and $\bar{G}$ have already been defined in Eqs. (15), and the Jacobian matrices $A$, $B$, $C$, and $M$ are described in detail by Pulliam and Steger.[12,13] The superscript $n$ indicates at which instant of time the quantity should be evaluated.

As usual with central differenced approximate factorization schemes, artificial numerical dissipation is necessary to maintain stability of the numerical solution process. In the right-hand-side operators, fourth-order numerical dissipation is used for the interior points and second order is used for the boundary points, except when operating in the $\zeta$ direction where fourth-order numerical dissipation is used for all points. The reason for the different treatment of the $\zeta$ direction is because this is the circumferential direction in this work, and, since a periodic grid is used in this direction, there is no reason to switch to second order at the boundaries. In the left-hand-side operators, second-order artificial dissipation is used everywhere in order to keep the matrices block tridiagonal, and so maintaining a cost-efficient solution algorithm. The amount of artificial dissipation introduced in each side is controlled by the coefficients $\varepsilon_E$ (for explicit) and $\varepsilon_I$ (for implicit), respectively, as indicated in the previous equations.

The computer code used in this work is a modification of the ARC3D code (in the public domain) set up to be vectorized and run on a CDC Cyber 205 computer. The theoretical formulation of the ARC3D code is described, among other references, by Pulliam.[8] The data base is structured in a pencil format that minimizes the amount of data that has to be kept in main memory at a given time. The pencil data structure concept, as well as the procedure for solving Eq. (16) when the data base has such a format, are described in detail by Deiwert and Rothmund.[11] Briefly, for each time step, the equation is solved by forming the right-hand side, and then inverting separately, in the sequence indicated, each of the left-hand-side operators, through the use of an LU (lower-upper) decomposition algorithm for block tridiagonal matrices. Again, since the grid in the $\zeta$ direction is periodic in the

present work, a periodic tridiagonal solver was programmed for that direction.

Although not explicitly mentioned in the previous equations, freestream subtraction is performed in the flux vectors when computing the right-hand terms in Eq. (16). The reason for this is that when arbitrary curvilinear coordinates and general finite differences are used, a small numerical error is introduced that may cause the code to be unable to reproduce the freestream (or a uniform flow). By performing the freestream subtraction in the flux vectors, we ensure the capability of recovering freestream and reduce the overall error of the method.

Since a viscous formulation is used here, at body walls we have no-slip boundary conditions, i.e., $u = v = w = 0$ for steady problems, or $u = x_\tau$, $v = y_\tau$, and $w = z_\tau$ for unsteady cases. We assume also adiabatic walls and zero normal pressure gradient at body walls. Uniform freestream is enforced at the upstream and far-field lateral boundaries. The treatment given to the downstream boundary depends on the value of the freestream Mach number. For supersonic freestream, the downstream boundary is extrapolated from interior values. For subsonic freestream, according to characteristic relations, there are four characteristics propagating downstream and one propagating upstream. To be consistent with that, pressure is then fixed at the downstream boundary (at its freestream value) and the other quantities are extrapolated from interior values. Finally, it should be mentioned that all the boundary conditions are treated explicitly in the present work.

## Aeroelastic Problem

The structural-dynamic equations for the vehicle are developed considering free-free flexural vibration of an elongated beam with variable properties and are cast in modal form. It is implicitly assumed here that the angle of attack remains low enough such that no lateral forces will appear, and so bending in only one plane has to be considered. Experimental results by Hsieh[14,15] seem to indicate that this assumption can be good even up to 19 deg incidence for general blunt body geometries.

The elastic deflection $\delta(x, t)$ at any station along the body can be represented by[16]:

$$\delta(x, t) = \sum_{i=1}^{\infty} q_i(t)\phi_i(x) \tag{17}$$

where $q_i(t)$ are the generalized normal coordinates and $\phi_i(x)$ are the normal modes.

Since the normal coordinates are not coupled either elastically or inertially, the equation of motion for each of the $i$th coordinates can be written as

$$\overline{m_i}[\ddot{q}_i(t) + 2\zeta_i\omega_i\dot{q}_i(t) + \omega_i^2 q_i(t)] = P_i(t) \tag{18}$$

Knowing the actual vehicle mass distribution, the generalized masses $m_i$ can be obtained from

$$\overline{m_i} = \int_{\text{body}} m(x)\phi_i(x)\phi_i(x)\,dx \tag{19}$$

All of this formulation is standard for any aeroelastic analysis and does not need to be discussed further. The only exception concerns the treatment of the generalized forces $P_i(t)$. These forces can be calculated as:

$$P_i(t) = \int_{\text{body}} l(x, t)\phi_i(x)\,dx \tag{20}$$

where $l(x, t)$ is the local lift per unit of length at station $x$ and time $t$, which can be obtained from a suitable circumferential integration of the pressure distribution around the body found by the flow solution described in the previous sections. So, although Eq. (18) looks like a linear equation, the true nonlinear character of the present analysis is hidden in the generalized aerodynamic forces.

Since the calculation of the flow solution at each time step, and therefore the evaluation of $P_i(t)$, is much more time consuming than the solution of the structural-dynamic equations, this poses some constraints on the numerical method that can be used for the time integration of Eq. (18). The idea of transforming the second-order equation into a first-order system as usually done in control theory may seem attractive, but it is not very practical in this case. For instance, any implicit method or any predictor-corrector sequence, which typically involves the evaluation of the forcing term at an instant of time ahead of the current time, would become prohibitive as far as the computational time is concerned with present computers. On the other hand, the explicit Euler method can be shown to be always unstable in the case by a simple linear stability analysis.

The procedure selected to advance Eq. (18) in time in the present work consists of a straight finite differencing of both the first and second time derivatives, as also done by Steger and Bailey,[17] Guruswamy and Yang,[18] and Borland and Rizzetta.[19] Using second-order-accurate formulas, those time derivatives can be approximated as

$$\ddot{q}_i \cong \frac{q_{i,n+1} - 2q_{i,n} + q_{i,n-1}}{(\Delta t)^2}$$

$$\dot{q}_i \cong \frac{q_{i,n+1} - q_{i,n-1}}{2\Delta t}$$

where the subscript $i$ refers to the mode considered and the subscript $n$ refers to the time level at which the quantity is evaluated. With the above formulas, the expression for $q_{i,n+1}$, i.e., the generalized deflection of mode $i$ at time $n + 1$, is given by

$$q_{i,n+1} = \frac{[2 - (\Delta t)^2\omega_i^2]q_{i,n} - (1 - \Delta t\zeta_i\omega_i)q_{i,n-1} + (\Delta t)^2 P_{i,n}}{(1 + \Delta t\zeta_i\omega_i)} \tag{21}$$

Linear stability analysis of the foregoing scheme shows that it is stable for the range of values of $\Delta t\omega_i$ consistent with accuracy requirements and for the range of values of $\zeta_i$ likely to be encountered for real structures. The analysis also shows that for $\zeta_i \to 0$ the scheme is numerically nondissipative, which is, of course, the expected result, since central differences are being used. This is important to avoid hiding physically unstable solutions due to numerical dissipation introduced by the method.

The coupling of the two sets of equations, the Navier-Stokes equations governing the flow behavior and the aforementioned structural-dynamic equations governing the oscillating vehicle behavior, is performed in the following way. At each time step, the aerodynamic equations are solved in a time-accurate fashion, and their solution provides the forcing terms for the aeroelastic analysis, which are weighted integrals of the pressure distribution along the body surface as was previously shown. Solution of the structural-dynamic equations gives the new deformed shape of the body as well as the body surface velocities and, therefore, the boundary conditions for the aerodynamic solution at the next time step. By tracing the growth or decay of a perturbed oscillation, the aeroelastic stability of a given configuration can be ascertained.

The solution process, as implemented here, recalculates the whole computational mesh at every time step to account for the deformation and motion of the body. This was done to provide greater generality to the method and enable it to treat larger deflections. In the present implementation of the method, the rigid body degrees of freedom were assumed to be somehow constrained, and only the elastic ones were considered. There is no additional conceptual difficulty in

including the rigid body modes in the current code, but results by Woods and Ericsson[1] seem to indicate that the inclusion, or not, of the rigid modes is not critical for determining the aeroelastic stability of a given vehicle.

## Results

Two different vehicle geometries were considered in this work. Initially the rigid body pitching of a hemisphere-cylinder geometry was considered, and the unsteady aerodynamic forces generated by this motion computed. Later, the aeroelastic stability of a hammerhead payload was addressed.

### Hemisphere Cylinder in Pitch Oscillation

Before attempting any true aeroelastic calculation, it was felt that it would be appropriate to try to validate the code developed against known results from the literature. A hemisphere-cylinder geometry was selected for these calculations, because results for this kind of geometry are more readily available in the literature, and also because being a simpler configuration would make it easier to pinpoint any possible problems in the code.

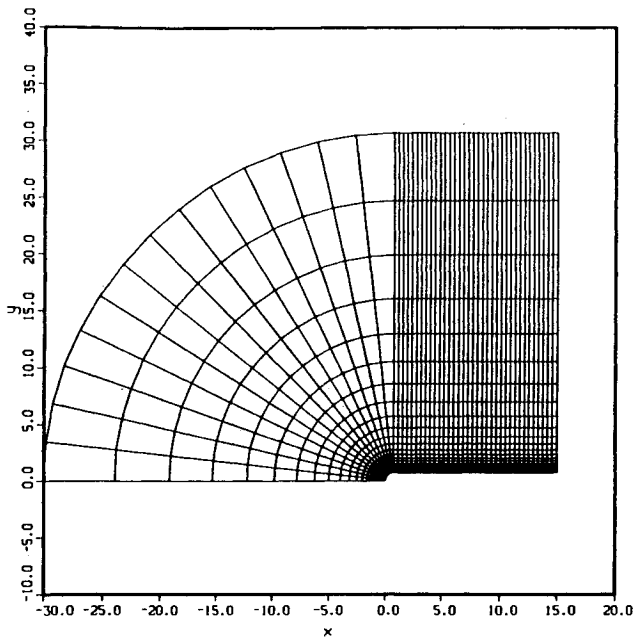


a) Longitudinal plane

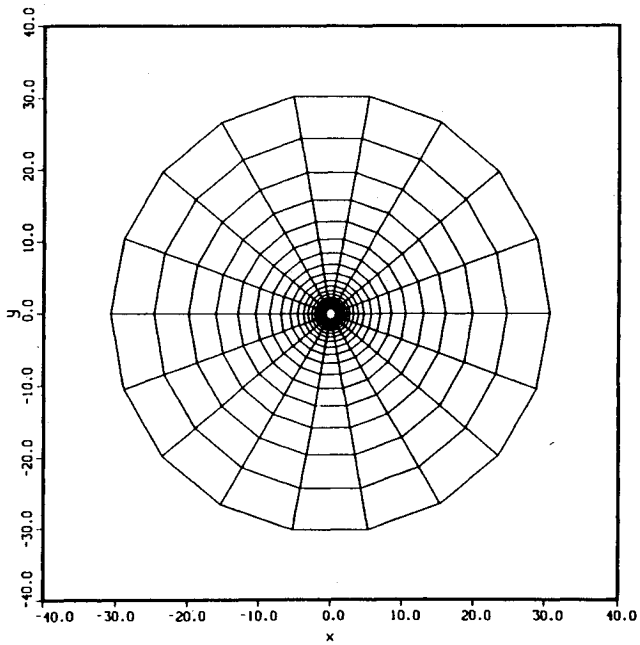


b) Crossflow plane

Fig. 1 Hemisphere cylinder typical grid plane.

The body conforming computational mesh was generated by algebraic methods, taking advantage of the simple vehicle topology. Grid lines run in the longitudinal, normal, and circumferential directions, and 50, 40, and 20 grid points were used, respectively, in each of these directions. A longitudinal grid plane is shown in Fig. 1a and a crossflow plane is shown in Fig 1b. Mesh points in the normal direction are clustered near the body in order to capture viscous effects, and a 25% exponential grid stretching is used in this direction. Over the hemispherical part of the body, grid lines in the longitudinal direction are placed at equal angles; over the cylindrical part of the body, those grid lines are equally spaced. Grid lines in the circumferential direction are generated by rotating one longitudinal plane at equally spaced angles around the body. Note that two circumferential planes are overlapped in order to facilitate the enforcement of the boundary conditions when operating in this direction.

Wind tunnel static pressure distributions presented by Hsieh[14] for a hemisphere cylinder are in the Mach number range of interest for this work, and so are used for these benchmark computations. Figure 2 shows a comparative plot of $Cp$ along the body surface for a flight Mach number $M_\infty = 0.6$, zero angle of attack, and the same Reynolds

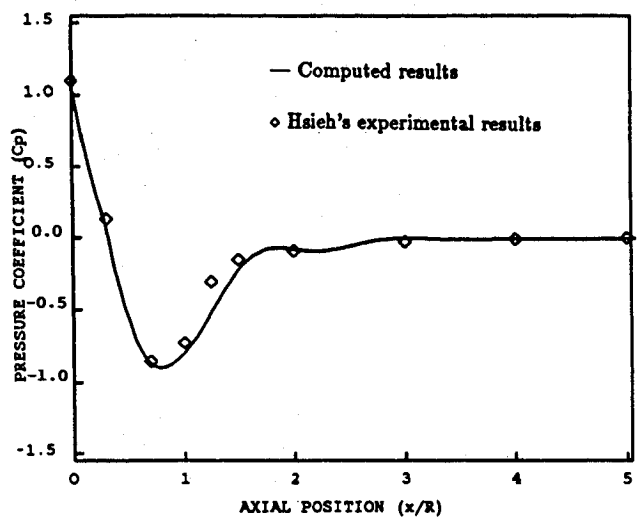


Fig. 2 Pressure coefficient distribution on hemisphere cylinder at $M_\infty = 0.6$ and zero angle of attack.

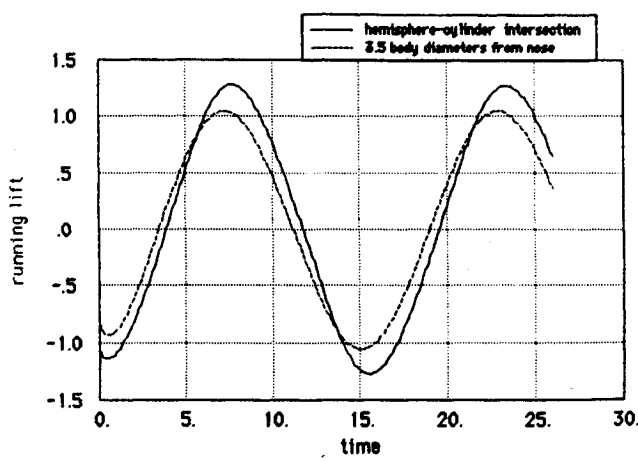


Fig. 3 Unsteady aerodynamic load on a hemisphere cylinder undergoing a sinusoidal pitching oscillation ($M_\infty = 0.6$, $\alpha = 0$ deg, $k = 0.4$, $\theta_0 = 5$ deg).

number as in Hsieh's experiments. For these calculations the turbulence model was turned off, such that these are laminar computational results. It can be seen that the computed results agree well with the experimental ones. The difficulty the computed results seem to have to recompress to the freestream pressure value after the minimum $Cp$ peak probably can be explained by the fact that the grid is indeed very coarse, and one may expect to have inaccuracies, especially in expansion regions. It should be noted also that this is a fully subsonic flow, i.e., there are no supersonic pockets in it. Again, the reason for not attempting a higher Mach number solution is that, with such a coarse grid, it would not be realistic to expect to capture shocks accurately.

Using this steady-state solution as a starting solution, the hemisphere cylinder was then subjected to a sinusoidal pitch oscillation. The reduced frequency of the oscillation is 0.4 (based on the diameter), and the half-amplitude angle of the oscillation is $\theta_0 = 5$ deg. The pitch axis was considered to be at the downstream boundary for the present calculations. Time histories of the running lift, i.e., the lift per unit of axial length, for two axial stations along the body are shown in Fig. 3. The distribution of the running lift along the body is shown in Figs. 4a and 4b for several instants of time along the oscillation. Unfortunately no experimental, or computational, results could be found to compare with the present calculations, but they seem to agree perfectly well with the kind of behavior that could be expected for this heavily forced oscillation.

From Figs. 3 and 4 we can see that the unsteady aerodynamic loads on the body lag the motion by a phase shift of almost 90 deg, and that the influence of the freestream angle of attack at any instant along the oscillation is very small in determining the total load at that time instant. In other words, the loads in phase with the motion are very small compared to the one induced by body oscillating velocities. Fig. 3 also shows that this phase lag decreases as we move from the forebody to the aft portion of the body. The reason for this behavior resides in the fact that we have a very high value of reduced frequency and, in this case, the velocities induced by the motion on the forebody are comparable to freestream velocities.

The high reduced frequency also explains why the initial transients die out so fast in this case, which can be seen from Fig. 5, where the running lift distribution along the body is shown for the same pitch position at two different cycles of the oscillation. The curves almost coincide, indicating that in this case after only a half-cycle of oscillation the initial transients have already died out. In summary, for such a heavily forced oscillation, we should expect to see the aerodynamic loads being determined primarily by the motion itself, and the present computations are indeed showing this feature.

It should be pointed out that the frequency of oscillation used in the foregoing investigation is about four times larger than one should realistically expect to find in flight. Experimental, or computational, results could not be found in the literature for the type of oscillatory motion we were interested in, regardless of the value of frequency considered. Therefore, the high value of reduced frequency was chosen mainly to allow for a faster turnaround time, while still permitting some qualitative study of the performance of the code.

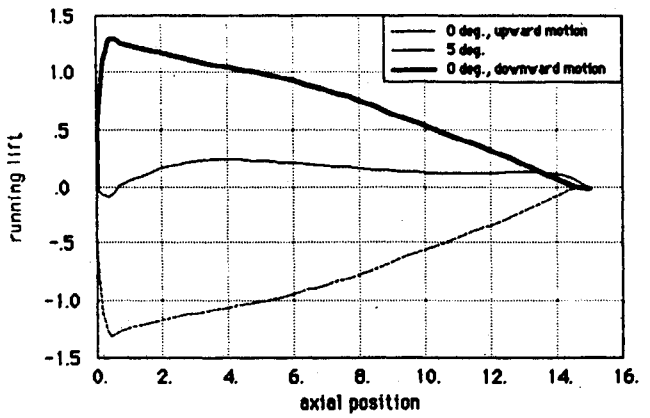


a) Distributions for $\theta = 0$ deg (upward and downward motions) and for $\theta = 5$ deg

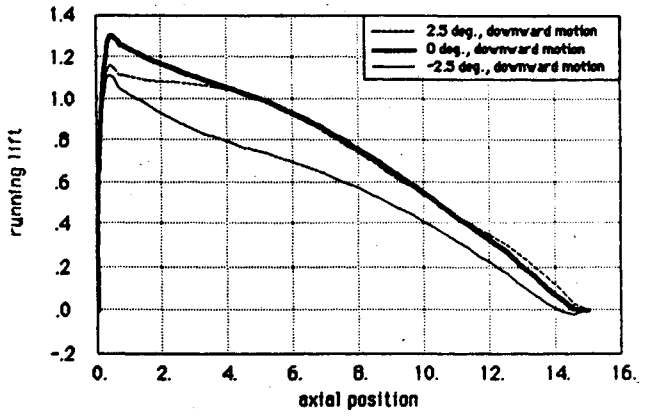


b) Distributions for $\theta = 2.5$, 0, and $-2.5$ deg, downward motion

**Fig. 4 Comparative plots of unsteady aerodynamic load distribution on hemisphere cylinder in pitch oscillation ($M_\infty = 0.6$, $\alpha = 0$ deg, $k = 0.4$, $\theta_0 = 5$ deg).**

### Aeroelastic Analysis of Hammerhead Payload

The computational mesh about a hammerhead payload geometry was also generated by algebraic methods. The grid has 105 points in the longitudinal direction, 66 points in the nearly normal direction, and 38 points in the circumferential direction. Again, once a longitudinal plane of the grid is generated, this plane is rotated through 360 deg to create the full three-dimensional grid. A longitudinal plane of the grid is shown in Fig. 6a, and Figs. 6b and 6c show details of forebody and flare regions, respectively. The $n$ direction in this case is being called the nearly normal direction because in the boattail and flare regions of the grid the $\eta$ lines do not intercept the body surface at 90 deg angles, as can be readily seen from the above-mentioned figures. However, numerical computations of boattail flowfields by Deiwert[20] indicate that this does not cause enough numerical problems to justify a more elaborate grid generation scheme, if the boattail (or flare) does not have a very steep slope.

In this case, since true transonic solutions are attempted, it is important to have a better clustering of the grid points along the body (in the longitudinal direction) in the regions where higher gradients are likely to occur. For this reason,

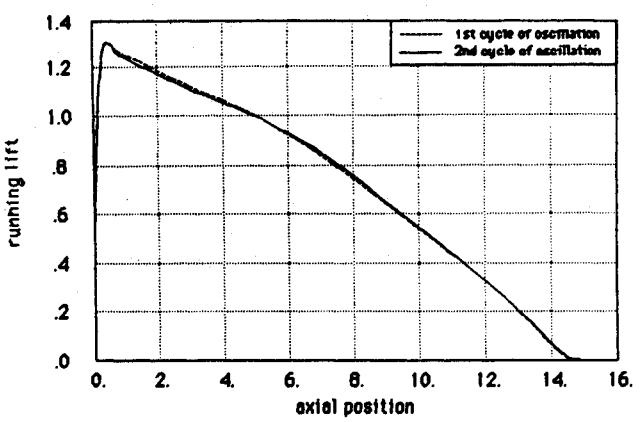


**Fig. 5 Unsteady aerodynamic load distribution on a pitching hemisphere cylinder at $\theta = 0$ deg (downward motion) for the first and second cycles of oscillation.**

one parameter, hyperbolic tangent grid stretching[21] is used to cluster the grid points around the hemisphere-forebody cylinder and the flare-afterbody cylinder intersections. To avoid wasting grid points in the downstream part of the afterbody cylinder where the flow is fairly simple, an 8.5% exponential stretching is used there to increase the grid spacing toward the downstream boundary. In the normal, or nearly normal, direction a 16% exponential grid stretching is used everywhere in order to cluster grid points near the body for capturing the viscous effects.

A steady-state flow solution was obtained over this geometry for a freestream Mach number $M_\infty = 0.85$, an angle of attack $\alpha = 6$ deg, and the Reynolds number $Re = 1.26 \times 10^6$ (based on the diameter). The boundary layer was considered turbulent and therefore the turbulence model was turned on. Leeside and windside pressure coefficient contours are shown in Figs. 7a and 7b, respectively. Similarly, leeside and windside pressure coefficient distributions on the body are shown in Figs. 8a and 8b, respectively. These pressure distributions seem to have all the features that would be expected, except that a more clearly defined shock was expected to be seen on the leeside of the forebody.

The preceding solution will be used as the starting flow solution for the aeroelastic cases studied here. Since this solution was calculated for a rigid vehicle, these airloads are not the actual loads at a deformed equilibrium position for the elastic vehicle. This provides a way of introducing the initial perturbation to start the oscillation, which will be adopted in the present work.

The structural information necessary for the present analysis consists of some normal mode shapes and their corresponding natural frequencies, the structural damping coefficients associated with each mode, and the vehicle mass distribution. Since no data for an existing vehicle could be found in the literature, an estimate was made of the necessary information from what was available in the literature so that the method being developed could be checked out. Unfortunately, this does not leave us with much to compare the results with, but it was felt that it was still worth the exercise in order to show what can be done once more realistic data can be obtained.

In the present analysis, three structural mode shapes were considered. These mode shapes were obtained from an extrapolation of the data presented by Woods and Ericsson,[1] and reasonable natural frequencies of vibration were assumed for each of these modes. In the first case run, all the structural damping coefficients were set to zero, and a very small value of dynamic pressure was considered. The objective in this case was to show that the numerical method was not introducing any numerical dissipation, or instability, and a pure sinusoidal response could be captured. The responses in terms of the generalized modal displacements in the second and third modes in this case are shown in Figs. 9a and 9b.

The second case considered a more realistic value of dynamic pressure and also the following values of structural damping coefficient: $\zeta_1 = 0.0010$, $\zeta_2 = 0.0018$, and $\zeta_3 = 0.0036$. The vehicle response is shown in Figs. 10a, 10b, 10c, and 10d, where the total elastic deflection, first, second, and third mode generalized coordinates are presented, respectively. The result shows that this vehicle, under the given flight condition, is free from aeroelastic instability.

Finally, something must be said about the computational costs of these aeroelastic solutions. For a $105 \times 66 \times 38$ grid, which was the case considered here, each iteration takes about 12 CPU seconds on a CDC Cyber 205 computer, which then implies that an aeroelastic solution such as the one shown in Fig. 10 costs about 3600 CPU seconds. Note, however, that this does not include the time necessary to generate the initial steady-state solution. If one is starting from uniform flow, the initial steady-state solution may be rather expensive, especially in the transonic flight regime. However, once one steady-state solution is obtained for a given flight condition,

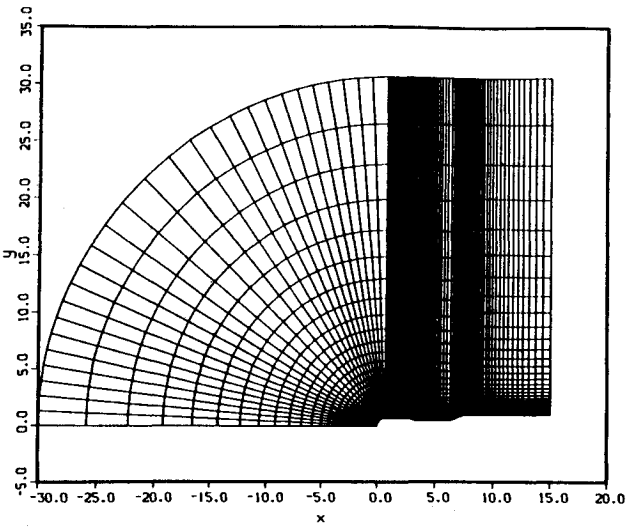


a) Complete plane

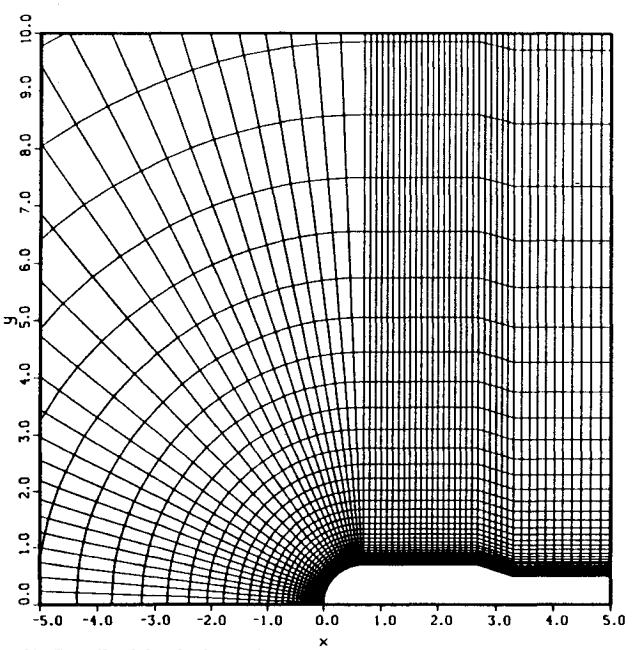


b) Detail of forebody region

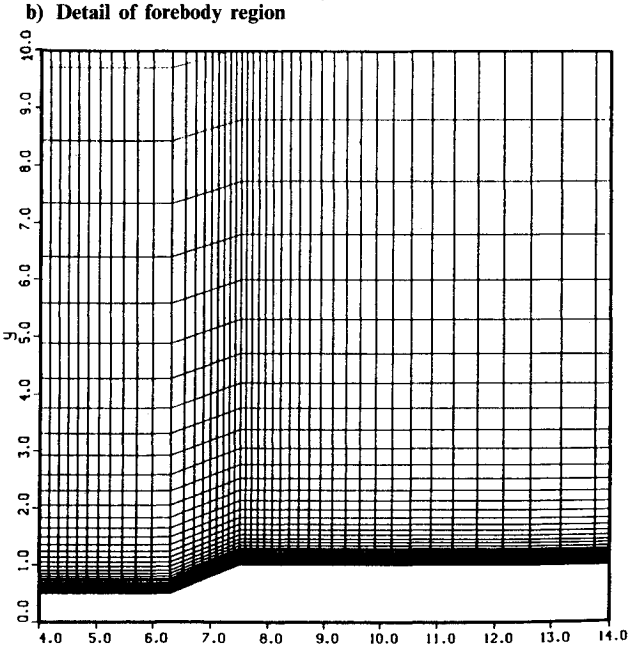


c) Detail of flare region

**Fig. 6 Typical longitudinal grid plane for hammerhead payload.**

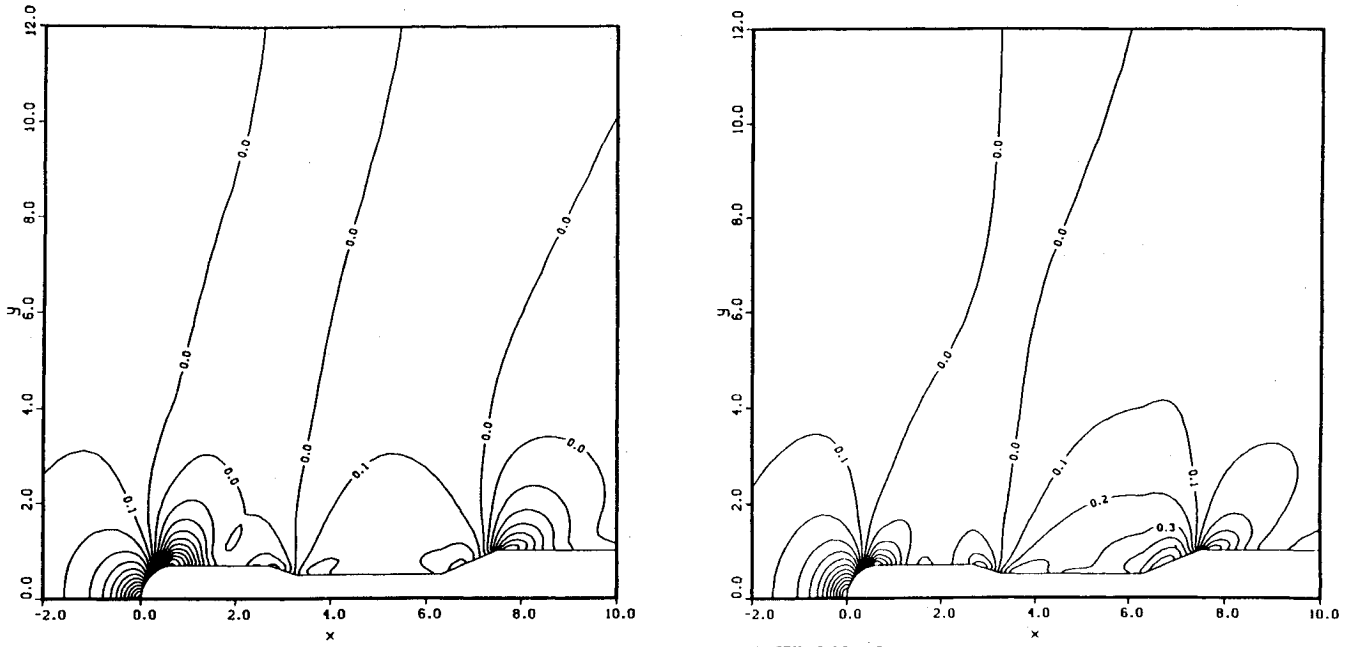


a) Leeside plane b) Windside plane

Fig. 7 Pressure coefficient contours for flow about a hammerhead geometry at $M_\infty = 0.85$, $\alpha = 6$ deg, and $Re_D = 1.26 \times 10^6$.

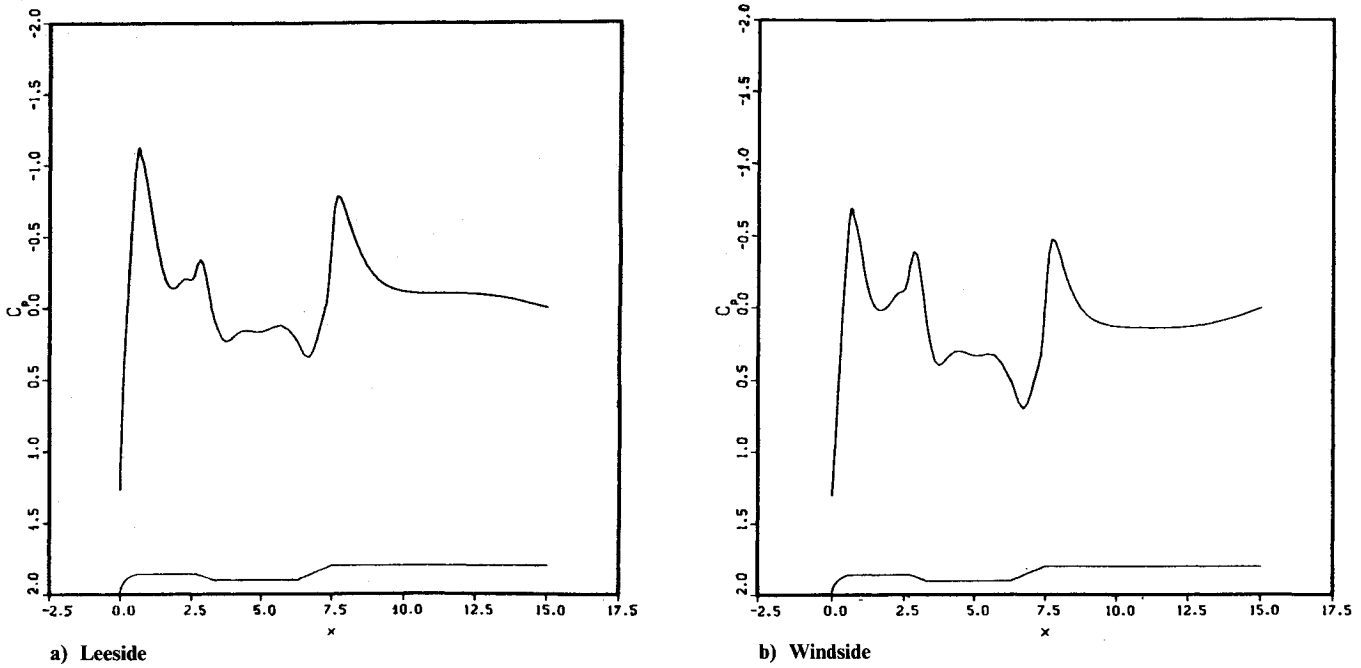


a) Leeside b) Windside

Fig. 8 Pressure coefficient distribution along the body for a hammerhead payload at $M_\infty = 0.85$, $\alpha = 6$ deg, and $Re_D = 1.26 \times 10^6$.

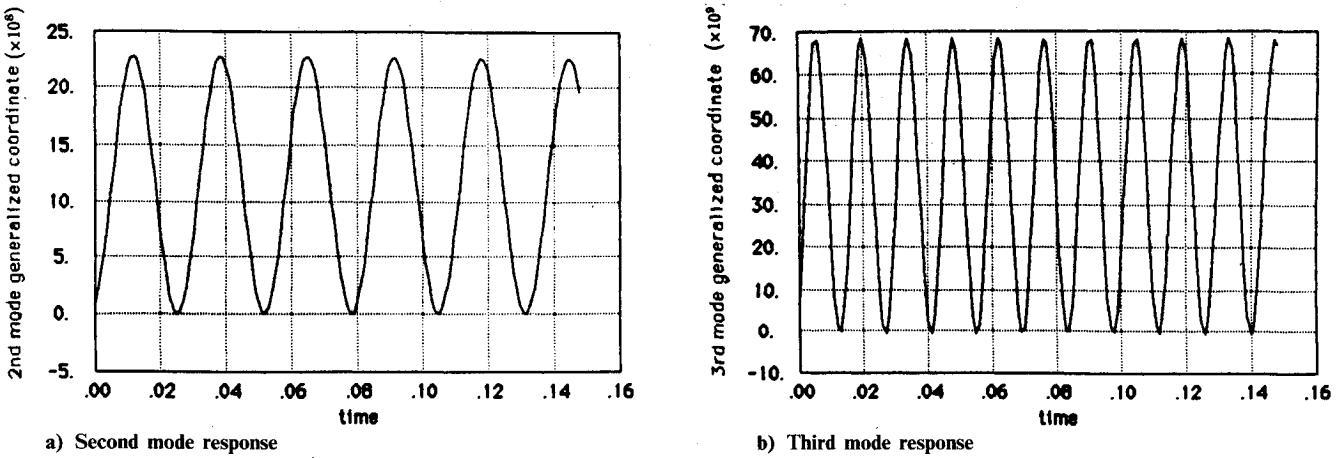


a) Second mode response b) Third mode response

Fig. 9 Response for zero structural damping and low dynamic pressure.

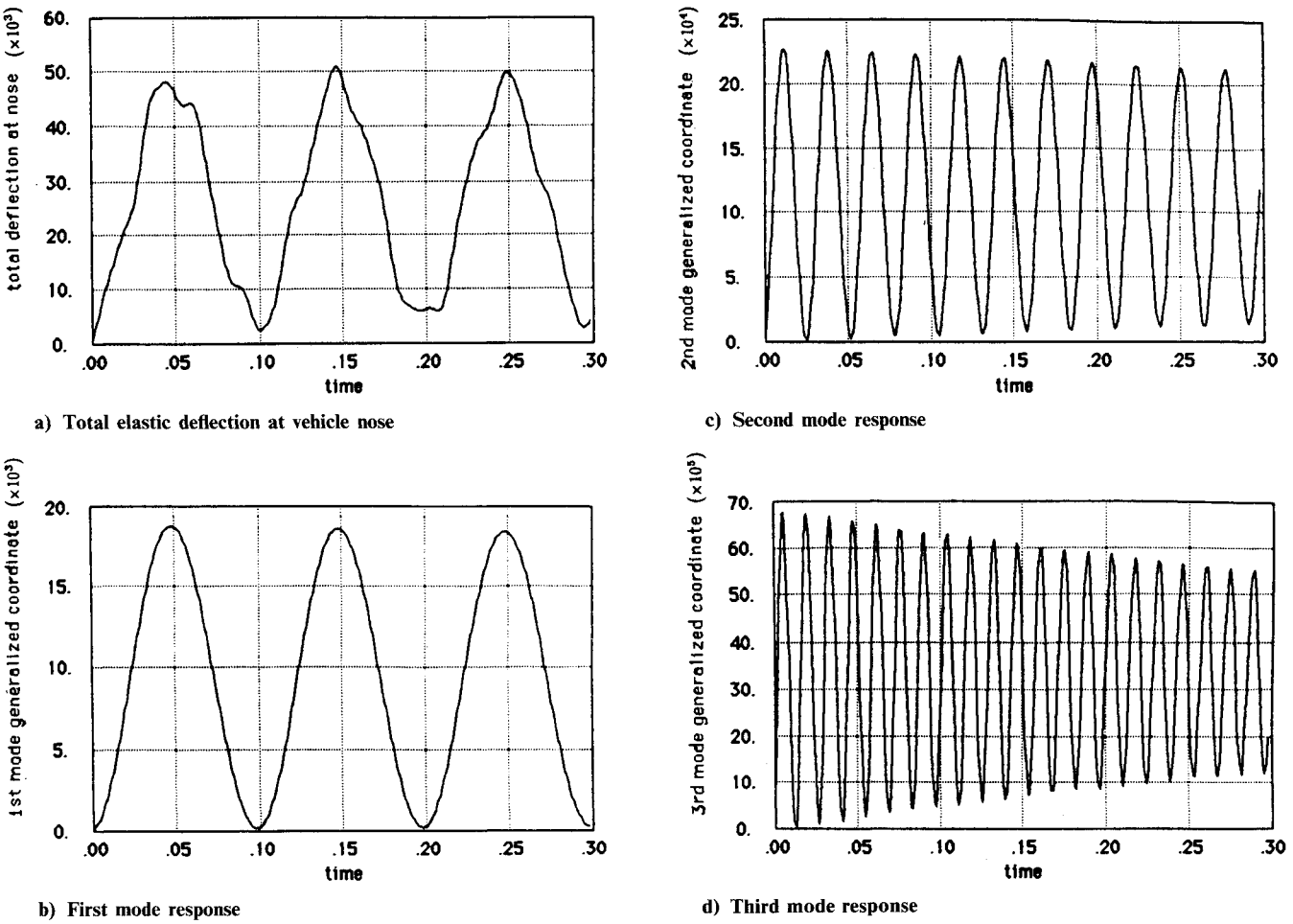


a) Total elastic deflection at vehicle nose

c) Second mode response

b) First mode response

d) Third mode response

**Fig. 10 Response of a stable configuration at $M_\infty = 0.85$.**

others can be generated for different flight conditions at a fraction of the cost since the previous solution can be used as a starting guess for the new one.

## Final Comments and Conclusions

Despite the fact that the idea of the present approach, in itself, is not new,[22] the contribution of this work is the demonstration of the use of the complete three-dimensional Navier-Stokes equations for the flow simulation and aeroelastic analysis of a realistic three-dimensional body configuration. This departs from work done in the past, where a potential formulation was used for the aerodynamic problem[19] or only two-dimensional problems were considered.[17] The results obtained so far seem to indicate that the method can indeed handle the class of problems we intended to address here. The analysis of problems with more realistic structural data and the comparison of the results with experiments, or with the results obtained by the semiempirical methods used so far,[1,3] however, is still necessary before any definite statement can be made about accuracy.

The structural-dynamic formulation presented considered that normal vibration modes for the vehicle are known. However, if those are not available, and the elastic modes available are coupled either elastically or inertially, this actually does not present any problem to the application of the present method. The difference would only be that instead of solving for each of the generalized modal coordinates separately, the solution would have to be done considering the (now) coupled system of equations. Since the number of structural modes that would be considered in a typical aeroelastic analysis is still extremely small compared to the size of the matrices involved in the solution of the aerodynamic problem, this would not significantly affect the overall computational cost of the solution.

It is true that the solution of the structural-dynamic part of the problem is a very small percentage of the overall solution time. However, one should note that there is a considerable cost increase per iteration when comparing a pure steady-state aerodynamic solution and an aeroelastic solution. This increase in computing time comes from the fact that, in an aeroelastic analysis, the body deforms, and so, in a general approach, the grid should be regenerated at every time step. That does not mean that the grid has to be regenerated from scratch at every time step, but some form of reshaping is definitely necessary, and the amount of time consumed for that is not necessarily trivial. In the present study, it was observed that the time per iteration increased by about 30% when going from a pure steady-state aerodynamic computation to an aeroelastic analysis.

Considering that the computational mesh is being regenerated at every time step in the present approach, probably an enhancement of the present code could be accomplished by incorporating some self-adaptive grid techniques[23,24] to the current algorithm. These techniques let the position of the grid points be driven by the solution, concentrating them on regions of higher gradients. The tradeoff usually involved is that by positioning the grid points in some optimum way, fewer points are necessary for a given accuracy. Thus, a faster run time is obtained. On the other hand, time is consumed to adapt the grid, which increases the total run time. Since in the present work the grid is already being reshaped at every time step, we probably would get only the advantages of self-adaptive grid methods without paying any additional costs.

The final issue that must be addressed is whether a computational procedure such as the one described here is already at

a stage where it can be used for routine aeroelastic clearance of a production vehicle. It should be noted that a fully nonlinear formulation like the one described here is not really necessary for the complete flight envelope. So, despite the fact that the computational requirements for the use of the present method are rather large, the author believes that the method can become an attractive option for aeroelastic analysis of a new vehicle in its transonic phase of flight, where the usual linearized methods break down. It should be kept in mind that the trend in the computer industry has been to develop larger and faster machines. Also, the constant improvements being achieved in numerical algorithms for the solution of fluid dynamic problems should not be overlooked. All this results in an effective reduction in computational costs, while the cost of experiments is definitely not being reduced.

## Acknowledgments

The author is indebted to Drs. H. Lomax and G. S. Deiwert for providing access to the NASA Ames Research Center computational facilities, as well as for very helpful discussions along the course of the work. The constant advice of Prof. Holt Ashley is also gratefully acknowledged. This research was partially supported by the Brazilian Government under a scholarship provided by Instituto de Atividades Espaciais, and partially supported by NASA under Grant NGL-05-020-243.

## References

[1]Woods, P. and Ericsson, L. E., "Aeroelastic Considerations in a Slender, Blunt-Nose, Multistage Rocket," *Aerospace Engineering*, Vol. 21, May 1962, pp. 42–51.

[2]Rainey, A. G., "Progress on the Launch-Vehicle Buffeting Problem," *Journal of Spacecraft and Rockets*, Vol. 2, May–June 1965, pp. 289–299.

[3]Ericsson, L. E. and Reding, J. P., "Fluid Dynamics of Unsteady Separated Flow. Part I. Bodies of Revolution," *Progress in Aerospace Sciences*, Vol. 23, Jan. 1986, pp.1–84.

[4]Baldwin, B. S. and Lomax, H., "Thin Layer Approximation and Algebraic Model for Separated Turbulent Flows," AIAA Paper 78-257, Jan. 1978.

[5]Anderson, D. A., Tannehill, J. C., and Pletcher, R. H., *Computational Fluid Mechanics and Heat Transfer*, McGraw-Hill, New York, 1984, pp. 479–502.

[6]Deiwert, G. S., "Supersonic Axisymmetric Flow over Boattails Containing a Centered Propulsive Jet," *AIAA Journal*, Vol. 22, Oct. 1984, pp. 1358–1365.

[7]Deiwert, G. A., Andrews, A. E., and Nakahaski, K., "Theoretical Analysis of Aircraft Afterbody Flows," AIAA Paper 84-1524, June 1984.

[8]Pulliam, T. H., "Euler and Thin Layer Navier-Stokes Codes: ARC2D, ARC3D," *Notes for Computational Fluid Dynamics User's Workshop*, Univ. of Tennessee Space Institute, Tullahoma, TN, March 1984.

[9]Chaussee, D. S. and Pulliam, T. H., "Two-Dimensional Inlet Simulation Using a Diagonal Implicit Algorithm," *AIAA Journal*, Vol. 19, Feb. 1981, pp. 153–159.

[10]Beam, R. M. and Warming, R. F., "An Implicit Finite-Difference Algorithm for Hyperbolic Systems in Conservation-Law Form," *Journal of Computational Physics*, Vol. 22, Sept. 1976, pp. 87–110.

[11]Deiwert, G. S. and Rothmund, H., "Three-Dimensional Flow Over a Conical Afterbody Containing a Centered Propulsive Jet: A Numerical Simulation," AIAA Paper 83-1709, July 1983.

[12]Pulliam, T. H. and Steger, J. L., "Recent Improvements in Efficiency, Accuracy and Convergence for Implicit Approximate Factorization Algorithms," AIAA Paper 85-0360, Jan. 1985.

[13]Pulliam, T. H. and Steger, J. L., "Implicit Finite-Difference Simulations of Three-Dimensional Compressible Flow," *AIAA Journal*, Vol. 18, Feb. 1980, pp. 159–167.

[14]Hsieh, T., "An Investigation of Separated Flows About a Hemisphere-Cylinder at Incidence in the Mach Number Range from 0.6 to 1.5," AIAA Paper 77-179, Jan. 1977.

[15]Hsieh, T., "Low Supersonic Flow over Hemisphere-Cylinder at Incidence," *Journal of Spacecraft and Rockets*, Vol. 14, Nov. 1977, pp. 662–668.

[16]Bisplinghoff, R. L., Ashley, H., and Halfman, R. L., *Aeroelasticity*, Addison-Wesley, Reading MA, 1955, pp. 67–131.

[17]Steger, J. L. and Bailey, H. E., "Calculation of Transonic Aileron Buzz," *AIAA Journal*, Vol. 18, March 1980, pp. 249–255.

[18]Guruswamy, P. and Yang, T. Y., "Aeroelastic Time Response Analysis of Thin Airfoils by Transonic Code LTRAN2," *Computers and Fluids*, Vol. 9, No. 4, April 1981, pp. 409–425.

[19]Borland, C. J. and Rizzetta, D. P., "Nonlinear Transonic Flutter Analysis," *AIAA Journal*, Vol. 20, Nov. 1982, pp. 1606–1615.

[20]Deiwert, G. S., "Numerical Simulation of Three-Dimensional Boattail Afterbody Flowfields," *AIAA Journal*, Vol. 19, May 1981, pp. 582–588.

[21]Vinokur, M., "On One-Dimensional Stretching Functions for Finite-Difference Calculations," NASA CR-3313, Oct. 1980.

[22]Nixon, D., "Prediction of Aeroelastic and Unsteady Aerodynamic Phenomena in Transonic Flow," *Unsteady Airloads and Aeroelastic Problems in Separated and Transonic Flow*, Lecture Series 1981–4, Von Kármán Institute for Fluid Dynamics, Rhode-Saint-Genese, Belgium, March 1981.

[23]Nakahashi, K. and Deiwert, G. S., "A Self-Adaptive Grid Method with Application to Airfoil Flow," AIAA Paper 85-1525, July 1985.

[24]Deiwert, G. S., Rothmund, H. J., and Nakahashi, K., "Simulation of Complex Three-Dimensional Flows," NASA TM-86773, July 1985.